

Cite this: *Mater. Horiz.*, 2020,  
7, 3275Received 1st August 2020,  
Accepted 21st October 2020

DOI: 10.1039/d0mh01240h

rsc.li/materials-horizons

# Bending good beats breaking bad: phase separation patterns in individual cathode particles upon lithiation and delithiation†

David A. Santos,<sup>‡,ab</sup> Justin L. Andrews,<sup>ib ‡,ab</sup> Yang Bai,<sup>‡,c</sup> Peter Stein,<sup>c</sup> Yuting Luo,<sup>ab</sup> Yuwei Zhang,<sup>d</sup> Matt Pharr,<sup>d</sup> Bai-Xiang Xu<sup>ib \*c</sup> and Sarbajit Banerjee<sup>ib \*ab</sup>

The operation of a Li-ion battery involves a concerted sequence of mass and charge transport processes, which are underpinned by alternating dilation/contraction of the active electrode materials. Several Li-ion battery failure mechanisms can be directly traced to lattice-mismatch strain arising from local compositional heterogeneities. The mechanisms of chemo-mechanical coupling that effect phase separation and the resulting complex evolution of internal stress fields remain inadequately understood. This work employs X-ray microscopy techniques to image the evolution of composition and stress across individual bent V<sub>2</sub>O<sub>5</sub> particles. Experimental findings show that lattice strain imposed by the deformation of an individual cathode particle profoundly modifies phase separation patterns, yielding striated Li-rich domains ensconced within a Li-poor matrix. Particle-level inhomogeneities compound across scales resulting in fracture and capacity fade. Coupled phase field modeling of the evolution of domains reveals that the observed patterns minimize the energetic costs incurred by the geometrically imposed strain gradients during lithiation of the material and illustrate that phase separation motifs depend sensitively on the particle geometry, dimensions, interfacial energetics, and lattice incommensurability. Sharp differences in phase separation patterns are observed between lithiation and delithiation. This work demonstrates the promise of strain-engineering and particle geometry to deterministically control phase separation motifs such as to minimize accumulated stresses and mitigate important degradation mechanisms.

## Introduction

Rechargeable Li-ion batteries are the preeminent energy storage technology for portable electronics and are poised to

### New concepts

The manuscript explores the fundamental materials science origins of why batteries fade upon repeated cycling. We examine the interplay between the crystal chemistry of intercalation reactions, particle geometry, and mechanical stresses accumulated at the single-particle level and illuminate how inhomogeneities that are entirely local and serve as stress concentrators ultimately compound across length scales resulting in the failure of full cells. The work presents: the first direct imaging of spinodal decomposition patterns in individual particles that have thus far only been conjectured through simulations; an examination of how bending a particle profoundly alters phase separation and stress concentration patterns; a demonstration of the role of geometric curvature and strain in resolving diffusion limitations; mapping of stress as a function of bending within individual particles and its cumulative consequences for full electrode architectures; and the fundamental materials science basis—elucidated at the level of single particles—for differences in charging and discharging processes. In summary, for the first time, we have examined the coupling of electrochemistry with mechanics at the single-particle level, and followed the evolution of accumulated stresses to entire electrodes, thereby delineating the fundamental mechanistic origins of failure in energy storage systems.

continue their dominance into emerging markets such as long-range electric vehicles and grid-level storage.<sup>1,2</sup> The function of Li-ion batteries is underpinned by a concerted sequence of mass and charge transport phenomena across numerous interfaces. The thermodynamic driving forces and dynamics of charge and mass transfer are dictated by the composition, atomistic structure, electronic structure, and mesoscale architecture of the individual battery components and their interfaces.<sup>3,4</sup> The cumulative effects that degrade the performance of full electrochemical systems originate at the level of

<sup>a</sup> Department of Chemistry, Texas A&M University, College Station, TX, 77843-3255, USA. E-mail: banerjee@chem.tamu.edu

<sup>b</sup> Department of Materials Science and Engineering, Texas A&M University, College Station, TX 77843-3255, USA

<sup>c</sup> Institute of Materials Science, Mechanics of Functional Materials, Technische Universität Darmstadt, Otto-Berndt-Str. 3, 64287 Darmstadt, Germany. E-mail: xu@mfm.tu-darmstadt.de

<sup>d</sup> Department of Mechanical Engineering, Texas A&M University, College Station, Texas 77840, USA

† Electronic supplementary information (ESI) available. See DOI: 10.1039/d0mh01240h

‡ These authors contributed equally to this work.

singular unit cells. In intercalation electrodes, lithiation often induces one or more structural phase transformations, dynamically altering lattice strain, Li-ion diffusion pathways, and electron localization of the host framework—even in the dilute limit of ion concentrations.<sup>4–6</sup> The limited miscibility of low- and high-lithiated phases in phase-transforming electrode materials poses a specific challenge and is the origin of phase separation and lattice coherency strain.<sup>7</sup> Solid-solution formation and phase-separation pathways are distinct manifestations of ternary phase diagrams. They are governed by the differential rates of (surface-limited) nucleation and phase propagation, and are further sensitive to the relative stabilities of the low- and high-lithiated phases, the commensurability of their crystal lattices, particle dimensions, and charge/discharge rates.<sup>8</sup> In this work, we use the distinctive X-ray absorption spectroscopy signatures of differently lithiated domains to map and contrast phase separation within individual particles of a  $V_2O_5$  model cathode material upon delithiation and lithiation, demonstrating the role of particle geometry, lattice incommensurability, and particle size in governing the phase separation patterns at equilibrium. We furthermore utilize compositional maps constructed using synchrotron scanning transmission X-ray microscopy (STXM) to generate a quantitative stress profile of individual particles, delineating the contours of elastic misfit strain resulting from phase heterogeneity, and illustrating the single-particle origins of bulk stresses developed within porous composite electrodes during electrochemical cycling.

### Mechanics–electrochemistry coupling in intercalation cathodes

Much recent attention has focused on the coupling of electrochemistry and mechanics within electrochemical energy storage systems considering that accumulated stresses and strains are often disruptive to interfaces and are culpable for initiating damage mechanisms that result in capacity fade upon extended cycling.<sup>9–12</sup> For instance, considerable attention has been devoted to electrochemistry–mechanics coupling in silicon anode materials wherein the alloying of lithium is accompanied by a substantial volume change (approaching 300% for silicon anodes).<sup>13,14</sup> While lattice dilation/contraction as a result of lithiation/delithiation in cathode materials is orders of magnitude smaller ( $\sim 2\text{--}8\%$ ),<sup>15</sup> continuous strains on the order of 0.1–2% produce significant stresses that accumulate during discharge/charge processes. These stresses inevitably cause considerable damage as a result of the characteristically brittle nature of oxides which are the predominant class of intercalation hosts.<sup>12,15–17</sup>

Mitigating common degradation mechanisms to enable prolonged Li-ion battery cycling requires consideration of the close coupling between mechanics and electrochemistry.<sup>11,16,18</sup> Essentially, stresses accumulate within particles as a result of lithiation/delithiation inhomogeneities and the resulting lattice mismatch between differently lithiated phases.<sup>19,20</sup> Stresses within composite electrodes derive from intra-particle lattice mismatch as well as the inhomogeneous deformation of the surrounding matrix resulting from intercalation/de-intercalation-induced volumetric expansion/contraction of the particles. Several strategies have been implemented in pursuit of extended

chemo-mechanical stability, including scaling active materials below a critical size to circumvent lithiation and stress gradients;<sup>21</sup> chemical modification *via* alloying (to incorporate a secondary phase as a stress buffer);<sup>22,23</sup> and the design of mechanically robust three-dimensional nano-architected materials that resist plastic deformation and pulverization.<sup>24–26</sup>

The interplay between chemistry and mechanics allows the potentially beneficial aspects of using particle geometry and the resultant internal stress characteristics as a vector to control electrochemistry and to define phase propagation fronts. Strain-induced modulation of band structure is commonly utilized to enhance the mobility of charge carriers in semiconductors, but its application to electrochemical systems remains poorly understood.<sup>27–30</sup> Kim *et al.* developed a new class of energy harvesters from two partially lithiated Si films separated by an electrolyte-containing film wherein bending-induced asymmetric stress generated a chemical potential difference that allowed for diffusion of Li-ions along the induced stress gradient.<sup>31</sup> Pint and co-workers have shown that applying modest uniaxial elastic strains ( $< 2\%$ ) can increase the lithium diffusion coefficient more than two-fold in  $V_2O_5$  thin film cathodes.<sup>17</sup> However, unraveling the specific mechanisms of chemo-mechanical coupling is necessary to realize the promise of strain engineering in full measure. In the following sections, we implement hyperspectral X-ray imaging techniques, coupled with phase-field models to investigate strain-modulated diffusion and transformation characteristics in elastically strained particles of  $V_2O_5$ .

### Lithiation inhomogeneities in $V_2O_5$ and their stress implications

Vanadium pentoxide ( $V_2O_5$ ) has been considered as a Li-ion intercalation cathode material since the early work of Whittingham<sup>32</sup> owing to its abundance of interstitial sites, accessibility of multiple redox couples ( $V^{5+}/V^{4+}$  and  $V^{4+}/V^{3+}$ ), and strongly enthalpic driving forces for Li-ion intercalation.<sup>4,32–34</sup>  $\alpha$ - $V_2O_5$  crystallizes in a layered-structure with orthorhombic symmetry ( $Pmnm$  space group; Fig. S1A, ESI<sup>†</sup>). Li-ion insertion in  $V_2O_5$  induces a series of displacive transformations that serve to reduce coulombic repulsions between inserted Li-ions and accommodate the increase in electron density brought upon by intercalation (Fig. S1A–D, ESI<sup>†</sup>). Upon initial lithiation ( $x < 1$  in  $Li_xV_2O_5$ ), the  $\alpha$ -,  $\epsilon$ -, and  $\delta$ -phases are stabilized within lithium concentration windows of *ca.*  $0.0 < x < 0.1$ ,  $0.3 < x < 0.7$ , and  $0.9 < x < 1.0$ , respectively (Fig. S1A–C, ESI<sup>†</sup>), and these transformations are entirely reversible.<sup>35,36</sup> Anisotropic distortions and volume expansion relative to pristine  $\alpha$ - $V_2O_5$  (approaching 12.8% volumetric expansion for  $\delta$ - $LiV_2O_5$ ) accompany these intercalation-induced transformations.<sup>15,35,37</sup> Higher extents of lithiation ( $x > 1$  in  $Li_xV_2O_5$ ) result in an irreversible transformation to the  $\gamma$ - $Li_xV_2O_5$  phase ( $1.0 < x < 2.0$ ). The puckered and rearranged  $V_2O_5$  framework characteristic of this phase is retained upon delithiation instead of reverting to the  $\alpha$ - $V_2O_5$  framework (Fig. S1D, ESI<sup>†</sup>). Still greater extents of lithiation stabilize the highly disordered  $\omega$ - $Li_xV_2O_5$  phase ( $x > 2.0$ ), which is

nominally crystallized in a rock salt structure but appears to have little in the way of long-range order.<sup>38,39</sup> Phase coexistence is an inevitable consequence of the  $\text{Li}_x\text{V}_2\text{O}_5$  phase diagram, and indeed the limited miscibility and lattice incommensurability of the differently lithiated phases are anticipated to give rise to considerable stress gradients, which in the case of continuous thin film electrodes can reach as high as several hundred MPa, resulting in cracking and delamination.<sup>15,40,41</sup>

The performance of  $\alpha\text{-V}_2\text{O}_5$  as a cathode is undermined by fundamental diffusion limitations arising from the formation of self-trapped polarons, phase heterogeneity, and irreversible energy dissipative phase transformations beyond  $x = 1.0$  in  $\text{Li}_x\text{V}_2\text{O}_5$ .<sup>42,43</sup> For porous electrodes combining active materials, binder, and conductive fillers, the effects of phase heterogeneity manifest as pronounced dips in Li-ion diffusivities<sup>43</sup> and capacity fade attributable to chemo-mechanical degradation mechanisms.<sup>15,37</sup> The extent of heterogeneity and spatial distributions of multiple lithiated phases provides a useful indicator of diffusion phenomena and allows for fundamental studies of electrochemistry–mechanics coupling in phase-separating electrode materials.<sup>8,19,42,44</sup>

In this work, we examine the effects of bending-induced strain on phase separation motifs using STXM measurements of individual  $\text{V}_2\text{O}_5$  particles to resolve distinctive lithiated domains and to develop quantitative phase maps. Phase heterogeneity is subsequently correlated to von Mises stress gradients through finite element analysis and phase-field modeling to examine the coupling between chemistry, mechanics, and geometry at the single-particle level in individual particles of  $\text{V}_2\text{O}_5$ , evidencing clear contrasts between lithiation and delithiation processes.

## Results and discussion

### Ensemble heterogeneity and accumulated stresses

Phase-pure  $\text{V}_2\text{O}_5$  nanowires have been grown by adapting a previously reported hydrothermal method, as described in the

Materials and Methods section.<sup>45,46</sup> The nanowires have an approximately rectangular cross-section with lengths on the order of several microns and widths of *ca.* 100 nm. Fig. S2 (ESI†) shows a powder X-ray diffraction pattern and Tables S1 and S2 (ESI†) note the refined lattice parameters and atom positions. Fig. S1F (ESI†) shows the charge/discharge profile acquired for this material, exhibiting plateaus corresponding to intercalation-induced phase transformations between the  $\alpha \leftrightarrow \varepsilon \leftrightarrow \delta \rightarrow \gamma$  phases, which follow the sequence of structural transformations sketched in Fig. S1A–D (ESI†). Structural transformations between the lithiated phases of  $\text{V}_2\text{O}_5$  at 3.39, 3.20, and 2.37 V, correspond to the  $\alpha \rightarrow \varepsilon$ ,  $\varepsilon \rightarrow \delta$ , and  $\delta \rightarrow \gamma$  transformations, respectively.<sup>43</sup> Fig. 1 illustrates the simultaneous potential and multi-beam optical stress (MOS) sensor measurements recorded concurrently for a composite electrode with  $\text{V}_2\text{O}_5$  active materials embedded within a matrix of conductive carbon and a polymeric binder. The cells are discharged in the voltage range of 4.0–2.0 V vs.  $\text{Li}/\text{Li}^+$  at 0.2C. The average stress change of the composite electrode ( $\Delta\sigma$ ) is inferred using Stoney's equation as per:<sup>47</sup>

$$\Delta\sigma = \frac{E_s h_s^2}{6h_f(1 - \nu_s)} \Delta K, \quad (1)$$

where  $E_s$  is the elastic modulus of the substrate ( $E_s = 203$  GPa),  $h_s$  is the substrate thickness ( $h_s = 0.736$  mm),  $\nu_s$  is Poisson's ratio of the substrate ( $\nu_s = 0.290$ ), and  $h_f$  is the thickness of the electrode material layer on the substrate ( $h_f = 42.3$   $\mu\text{m}$ ).

In just a few discharge/charge cycles, Fig. 1A shows that the sharpness of the reduction peaks is notably diminished and pronounced asymmetry begins to emerge, thus evidencing increased heterogeneity. In lockstep with Li-insertion (extraction), the  $\text{V}_2\text{O}_5$  electrode dilates (contracts) in the in-plane direction while constrained by the substrate and thus experiences compressive and tensile stress during lithiation and delithiation, respectively. Furthermore, the magnitude of the peak compressive and tensile stress increases approximately linearly with each cycle, evidencing a correlation between increasing phase

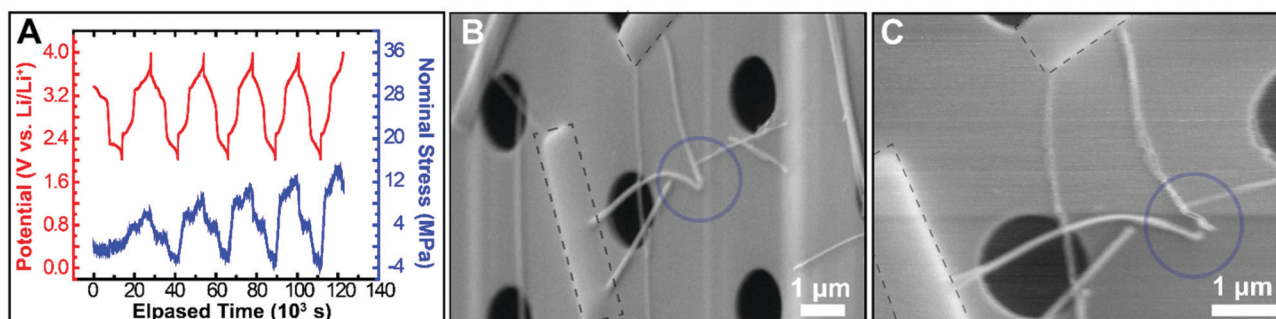


**Fig. 1** Stress accumulation and fracture of  $\text{V}_2\text{O}_5$  particles upon lithiation/delithiation. (A) Ensemble potential measurements and corresponding stress response during 5 galvanostatic cycles of a composite electrode embedded with  $\text{V}_2\text{O}_5$  particles between 4.0–2.0 vs.  $\text{Li}/\text{Li}^+$  at a current density of  $5.92 \mu\text{A cm}^{-2}$  (0.2C). The peak compressive and tensile stress response increases approximately linearly with each successive cycle. Here the sign convention for compressive and tensile stress is negative and positive, respectively. (B) SEM image of a pristine  $\text{V}_2\text{O}_5$  nanowire that has been mechanically affixed to a silicon nitride window by ion-beam ( $\text{Ga}^+$ )-assisted Pt deposition (deposited Pt strips are outlined by the gray dashed line) in a highly strained configuration. (C) The same nanowire shown in (B) following chemical lithiation/delithiation treatment to approximate the electrochemical cycling shown in (A). A cleavage of two strands is observed at the apex of the bend.

heterogeneity and accumulated stress in the electrode, both of which are amplified with extended cycling. Notably, the stresses here reflect the ensemble response of the composite electrode, the inherent porosity of which allows for partial accommodation of stresses developed in individual elements. Indeed, the overall stress magnitudes within individual elements can reach several hundred MPa, as evidenced by MOS studies of continuous  $V_2O_5$  films.<sup>15</sup> It is important to note that the stabilization of phase boundaries contributes to a “feedback-loop” wherein local inhomogeneities engender further heterogeneity through uneven local current densities and by establishing phase boundaries that inhibit Li-diffusion. Up to four orders of magnitude decrease in Li-ion diffusivity is observed as a consequence of phase coexistence regimes in  $V_2O_5$ .<sup>43</sup> Given the close coupling of phase boundaries and the resulting stress gradients, the compounding heterogeneities can continually undermine the chemo-mechanical integrity of the electrode particles.

Fig. 1B shows a scanning electron microscopy (SEM) image collected for a bent nanowire mechanically affixed on a silicon nitride substrate by ion-beam-induced Pt deposition. After a single chemical lithiation/delithiation cycle, a fracture is observed at the apex of the bend, resulting in cleavage into two individual strands (Fig. 1C) and illustrating an example of intercalation induced stress and fracture.

### Imaging single-particle lithiation heterogeneities

Recent X-ray diffraction and Raman microprobe measurements have found considerable phase heterogeneity across ensembles of  $V_2O_5$  particles upon lithiation/delithiation.<sup>45</sup> Synchrotron-based X-ray spectromicroscopy experiments have shown that inhomogeneities in both  $Li_xV_2O_5$  and  $Li_xFePO_4$  exist not just between different particles of an ensemble but also as domains within an individual particle.<sup>4,41,42,48,49</sup> The spatial distribution of compositionally distinct domains and phase separation patterns (as well as their dynamical evolution) are sensitive to lithiation conditions, particle size, morphology, and inter-connectivity.

The insertion of a Li-ion into a host material is necessarily accompanied by a redox event on the host lattice which strongly modifies the electronic structure. In electron-correlated transition-metal oxides with large bandgaps, the coupling of structural distortions to localized electron density gives rise to the stabilization of small polarons, which subsequently trap Li-ions.<sup>4,42</sup> The spectroscopic signatures of small polarons and localized electron density in hybrid V 3d–O 2p states provides a means to use STXM to map differently lithiated domains within  $V_2O_5$ .<sup>19,46,50</sup> In STXM, a user-defined region of interest is raster-scanned across a range of incident X-ray energies that correspond to relevant elemental absorption edges of the material. For each energy point  $E$ , a single image is generated by the two-dimensional array of pixels  $(x,y)$ , and their corresponding absorbance value,  $I$ , or collectively  $I(x, y, E)$ . A hyperspectral “stack” can be generated by superimposing X-ray images in ascending order of their incident photon energy; next, a full absorption profile can be created for each pixel by plotting the energies against their corresponding intensity. The spatial

resolution of STXM is on the order of a few tens of nanometers, providing a means to resolve electronic structure heterogeneities at the nanoscale.<sup>50</sup> In this work, the absorption of  $V_2O_5$  nanowires has been mapped across the vanadium L- and oxygen K-edges. Using stoichiometrically lithiated  $Li_xV_2O_5$  XAS “standards” as shown in Fig. S3 (ESI<sup>†</sup>), the extent of lithiation of the ROI, PCA, and SVD-derived spectra shown in Fig. 2C, D, 3A–C and 5A–C and throughout this work can be reasonably inferred; this is achieved by comparison of the evolution of the spectral signatures of the standards (V  $L_{3-}$  and O K-edge features) with increasing lithiation with the observed spectra. This approach has been successfully applied to deduce Li content in  $V_2O_5$  particles with different morphologies.<sup>26,42</sup>

### Imaging single-particle lithiation heterogeneities upon delithiation

Nanowires often adhere to the silicon nitride substrate in a bent configuration where they are held in place as a result of substrate interactions, enabling the same active element to be separately imaged by SEM and STXM (Fig. 2). Chemical lithiation (using *n*-butyllithium) and delithiation (using nitrosonium tetrafluoroborate) have been utilized as proxies for electrochemical discharge and charge processes.<sup>51,52</sup> The chemical lithiation/delithiation method employed here, greatly reduces the limitations that arise from limited wetting of cathode particles during electrochemical cycling.<sup>53</sup> Furthermore, a high molar excess of *n*-butyllithium and nitrosonium tetrafluoroborate have been utilized to ensure a large chemical overpotential and a constant thermodynamic driving force for intercalation/deintercalation.<sup>54</sup> The set of particles illustrated in Fig. 2A was lithiated and subsequently delithiated for a total of five cycles. After each lithiation and delithiation step, ample relaxation time was allotted to allow for the system to phase separate under equilibrium conditions and in the presence of the bending-induced strain. Fig. 2B shows the integrated optical density STXM image.

Several regions-of-interest (ROI) have been defined corresponding to distinct particles, as indicated by the colored and shaded regions in Fig. 2A superimposed on a SEM image. The corresponding spectral profiles are organized from bottom-to-top by increasing levels of lithiation ( $x$  in  $Li_xV_2O_5$ ) in Fig. 2C (based on comparison to the standards shown in Fig. S3, ESI<sup>†</sup>). The X-ray absorption near-edge structure (XANES) spectra shown in Fig. 2C comprise element-specific V L- and O K- absorption edges. The V L-edge comprises two features centered at *ca.* 518 eV (V  $L_3$ ) and *ca.* 525 eV (V  $L_2$ ), which are split by spin-orbit coupling of *ca.* 7 eV. The V  $L_3$ -edge (Fig. 2D) corresponds to transitions from V  $2p_{3/2}$  core levels  $\rightarrow$  V 3d states and is further characterized by fine features representative of the bottom of the conduction band. The features at *ca.* 515.6 eV and 516.8 eV correspond to V  $2p \rightarrow$  V  $3d_{xy}$  and V  $2p \rightarrow$  V  $3d_{xz/yz}$  transitions, respectively.<sup>42,55</sup> With increasing lithiation and formal reduction of vanadium centers, previously unoccupied V 3d orbitals are filled by electrons. This results in darkening (Pauli blocking) of the V  $3d_{xy}$  and  $3d_{xz/yz}$  features as evidenced in the spectra for stoichiometrically lithiated  $Li_xV_2O_5$

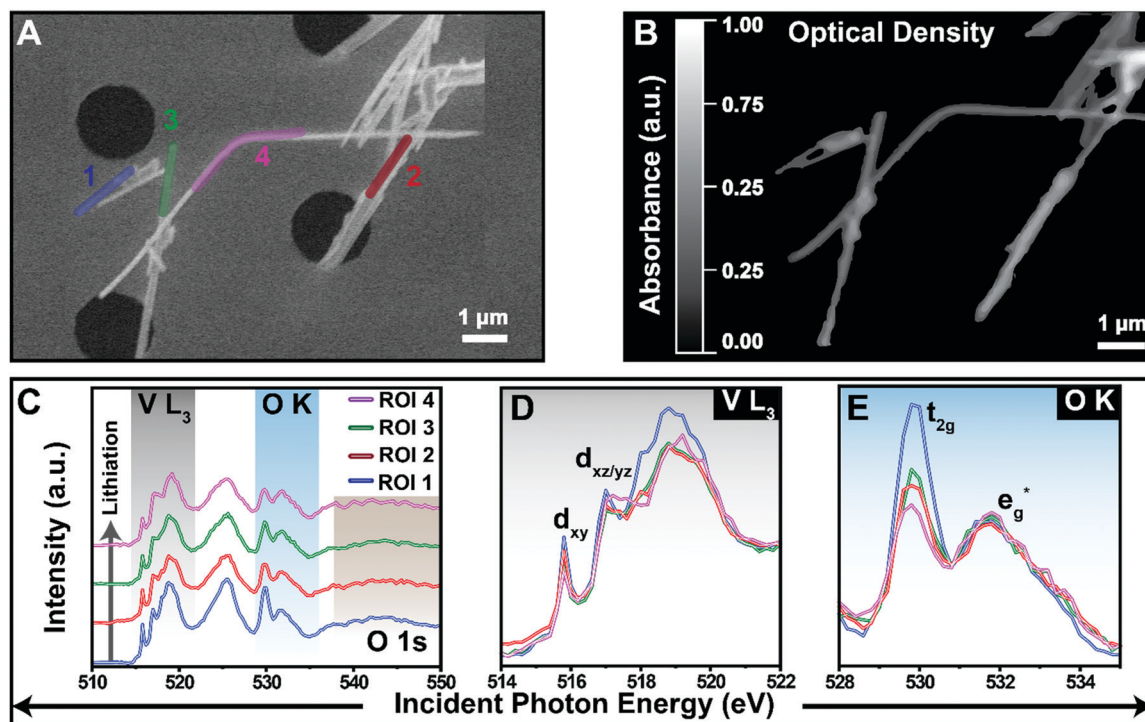


Fig. 2 Imaging single-particle lithiation heterogeneities. (A) SEM image of several interconnected  $V_2O_5$  nanowires with regions of interests 1–4 demarcated by blue, red, green, and magenta highlights, respectively. (B) STXM optical-density image collected for the same area as shown in (A). (C) Spectra obtained by a region-of-interest (ROI) analysis arranged in order of increasing average extent of lithiation (bottom to top). (D) Expanded view of the  $V L_3$ - and (E)  $O K$ -edge regions of the spectrum showing modification of specific spectral signatures with increasing lithiation.

standards plotted in Fig. S3B (ESI†).<sup>42,55</sup> The  $V L_2$ -edge (521–529 eV) is dominated by a Coster–Kronig Auger decay process into the  $2p_{3/2}$  holes, which obscures any fine structure features that would provide insights into electronic structure modulation.<sup>42,55</sup> The  $O K$ -edge XANES spectra (Fig. 2E) contain fine-structure features at *ca.* 529 eV ( $t_{2g}$ ) and 531 eV ( $e_g^*$ ), that correspond to transitions from  $O 1s$  core states to  $O 2p$  states hybridized with  $V 3d$  states. These hybrid states are split into two manifolds as a result of crystal field splitting in a distorted octahedral symmetry. Once again, the relative intensities of the  $t_{2g}$  and  $e_g^*$  features are found to be strongly dependent on the extent of lithiation (Fig. S3C, ESI†).<sup>42</sup> Upon lithiation, the intensity of the  $t_{2g}$  absorption is decreased relative to the absorption intensity of the  $e_g^*$  feature as a result of (1) electron correlation effects and the loss of degeneracy of spin-up and spin-down states and (2) distortion of the vanadyl moiety owing to  $Li$ – $O$  interactions; as a result of the longer  $V$ – $O$  bonds in lithiated  $V_2O_5$ ,  $V 3d_{xz}$  states are shifted to higher energies, reducing the spectral weight of the  $t_{2g}$  manifold and giving rise to a high-energy shoulder.<sup>42</sup> It is important to note that in the  $\delta$ - $Li_xV_2O_5$  phase (observed at extents of lithiation,  $x > 0.9$ ) there is a renormalization of the relative  $t_{2g}$  to  $e_g^*$  intensity. As a result of the structural rearrangement across the  $\epsilon \leftrightarrow \delta$  phase transition (Fig. S1E and highlighted in greater detail in Fig. S4, ESI†), the  $VO_{5+1}$  distorted octahedral coordination environment changes to an entirely square pyramidal coordination environment; the resulting change in crystal field splitting results in a substantial change of the  $O K$ -edge manifold in XANES spectra, as also evidenced in

the  $O K$ -edge XANES spectra collected for stoichiometrically lithiated  $Li_xV_2O_5$  standards shown in Fig. S3C (ESI†). The relative intensities of the fine structure features at the  $V L_3$  and  $O K$ -edges thus serve as a sensitive nanoscale probe of electron localization and the extent of lithiation.

Despite identical lithiation/delithiation conditions for the particles shown in Fig. 2, substantial compositional heterogeneity is evident when comparing spectral signatures for different nanowires (Fig. 2D and E). The spectrum corresponding to ROI 1 reflects the least lithiated region. The spectral signatures are indeed characteristic of an entirely delithiated  $\alpha$ - $V_2O_5$  particle.<sup>37,42,43,56,57</sup> Modest changes to the  $t_{2g}/e_g^*$  ratios at the  $O K$ -edge, observed in ROI 2 and ROI 3 (Fig. 2E), are typical of the low-lithiated  $\alpha$ - $Li_{0.1}V_2O_5$  phase, which is characterized by slight puckering of the layers during the insertion process. A more pronounced modification of the  $O K$ -edge is observed in ROI 4 (the curved portion of the particle) and points to a notably greater extent of lithiation. This is further corroborated by a diminished-intensity of the  $3d_{xy}$  feature in the  $V L_3$ -region; both spectral signatures thus attest to the stabilization of domains with higher remnant lithiation at the bent region of the nanowire, suggesting that the curvature of the wire significantly modifies strain fields in the vicinity of the curve.<sup>42</sup> In the following sections, we extend our analysis to include a closer look at heterogeneity within individual particles and the resulting stresses that arise due to lattice mismatch.

While a supervised ROI analysis provides a clear view of heterogeneity across ensembles of particles, unraveling the

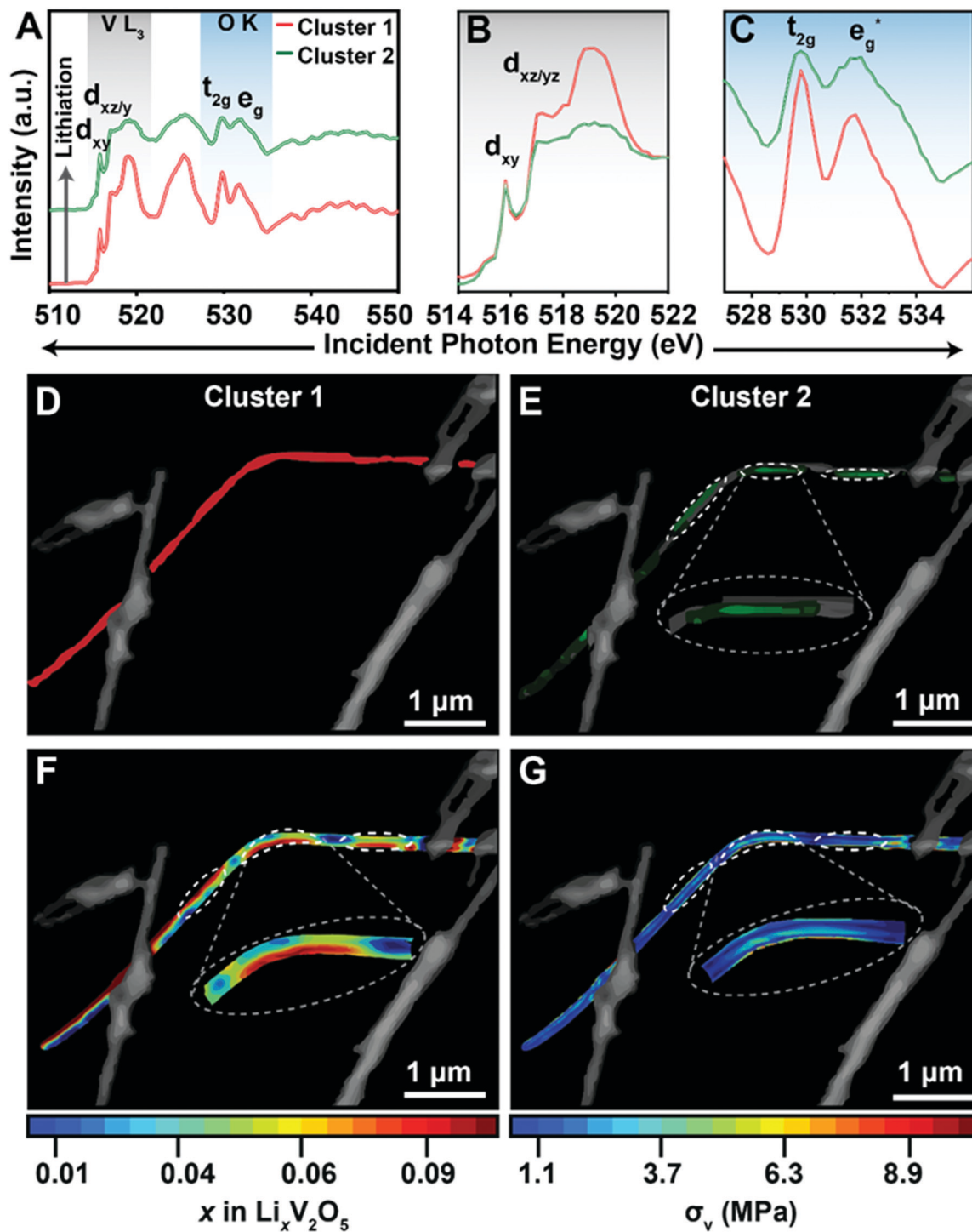


**Fig. 3** Compositional domains and resulting stress gradients within a bent nanowire upon delithiation. (A) Spectra obtained by averaging the spectral response of every pixel belonging to a pixel cluster as differentiated by a combinatorial PCA/clustering process. Spectra are plotted in order of increasing average extent of lithiation (bottom to top). Panels (B) and (C) highlight the lithiation-induced changes across V  $L_{3-}$  and oxygen K-pre-edge regions, respectively. The spatial orientation of each pixel contained in cluster 1 and cluster 2 is illustrated by red and green highlights in (D) and (E), respectively. The composition map derived according to the procedure detailed in the Materials and Methods is shown in (F). The stress profile derived from the apparent heterogeneity is illustrated in (G). Li-Rich striations occurring at the onset of the curvature and magnified views one of the striations are highlighted by dashed lines in (E–G).

complex spatial distribution of distinctive  $\text{Li}_x\text{V}_2\text{O}_5$  phases at the single-particle level is made possible by principal component

analysis (PCA) and iterative clustering; these tools enable deconvolution of the spectral signatures of differently lithiated

domains and their spatial localization.<sup>58–60</sup> Indeed, PCA and K-means clustering algorithms (as detailed in the Materials and Methods section) allow for compositionally distinct phases of  $\text{Li}_x\text{V}_2\text{O}_5$ , distinguished by the relative intensities of V  $L_3$  and O K-edge spectral features, to be resolved. The results of this analysis are presented in Fig. 3 and clearly show phase separation within the curved nanowire. Fig. 3A plots the cluster spectra; each spectrum represents a composite spectral response of all the pixels belonging to a singular cluster. Based on the intensity of the V  $L$ -edge pre-edge features and comparison to Fig. S3B (ESI<sup>†</sup>), both cluster spectra correspond to phases within the  $\alpha$ - and  $\epsilon$ -phase regions of the phase diagram. As discussed above, the relative intensity of the  $t_{2g}$  and  $e_g^*$  features at the O K-edge are expected to decrease with increasing extents of lithiation. Therefore, based on the relative decrease in the intensity of the V  $3d_{xy}$  feature at the V  $L_3$ -edge (Fig. 3B) and the reduced  $t_{2g}$  to  $e_g^*$  ratio at the O K-edge (Fig. 3C), cluster 2 is interpreted as having a higher degree of lithiation ( $x \sim 0.3$  in  $\text{Li}_x\text{V}_2\text{O}_5$ ). Fig. 3D and E illustrate the real-space distribution of the domains described by clusters 1 (red) and 2 (green), respectively. These intensity maps illustrate that the majority phase of the nanowire corresponds to a low-lithiated  $\alpha\text{-Li}_{0.1}\text{V}_2\text{O}_5$  phase with the exception of clear striations (represented in green in Fig. 3E) of Li-rich domains, which trace the presence of a Li-rich  $\epsilon\text{-Li}_{0.3}\text{V}_2\text{O}_5$  phase in the proximity of the bend in the nanowire. The Li-rich striations along the onset of the curvature represent a clear departure from the core-shell motifs observed in straight  $\text{V}_2\text{O}_5$  nanowires without comparable curvature.<sup>41,42</sup> The striations cannot be explained by a bending-induced asymmetric lithiation of the inner- and outermost edges of the nanowire as observed in other systems. We posit that the formation of distinctly lithiated domains along the length of the nanowire is indicative of an equilibrium state that minimizes the free energy of the system by balancing elastic strain gradients (induced by the static bend) and the lithiation-induced stress, which results from elastic misfit strain at the interfaces between high- and low-lithiated phases (*vide infra*).

Given the direct relationship between phase heterogeneity and stress gradients, we have utilized the STXM hyperspectral images along with thickness information derived from optical density data to develop quantitative composition maps as described in the Materials and Methods section.<sup>61</sup> Briefly, the averaged spectrum for each cluster is utilized as an input for singular value decomposition (SVD) analysis. In SVD, each pixel is described by a single intensity and a weighting factor of corresponding to extent of lithiation ( $x$  in  $\text{Li}_x\text{V}_2\text{O}_5$ ) thereby enabling the generation of a composition map as plotted in Fig. 3F.<sup>60</sup> The compositional map reproduces the observed periodic Li-rich domains of  $\epsilon\text{-Li}_x\text{V}_2\text{O}_5$  along the curve of the wire. The resulting matrix has been used to generate a finite element model from which stress distributions have been deduced, as shown in Fig. 3G.

The von Mises stress maps indicate that regions of high von Mises stress coincide with highly lithiated domains. Indeed, the observed stresses, which form a clear segmented pattern along the curve of the nanowire (as highlighted in the inset to

Fig. 3G), derive from compression of expanded Li-rich regions  $\epsilon\text{-Li}_x\text{V}_2\text{O}_5$  against the relatively low-lithiated domains of  $\alpha\text{-Li}_{0.1}\text{V}_2\text{O}_5$ . This coherency strain arises at the boundary between the two phases with vastly different extents of lithiation owing to lattice mismatch as a result of the different partial molar volumes of the two phases. The formation of a coherent interface implies that the adjoining phases have been strained to maintain coherency (as opposed to the relaxation of stored elastic energy through defect formation or cracking when the accumulated stresses exceed a certain threshold). When considered from the perspective of atomistic structure, the  $\alpha$ - to  $\epsilon\text{-Li}_x\text{V}_2\text{O}_5$  phase transition is characterized by the local expansion of the interlayer spacing in  $\text{V}_2\text{O}_5$  and the puckering of apical V=O bonds of the  $[\text{VO}_5]$  square pyramids as a result of the increased electrostatic interactions between the oxygen lone pair electrons and Li-ions (Fig. S1B, ESI<sup>†</sup>). This results in anisotropic expansion of the lattice along the crystallographic  $b$ -axis and contraction of the lattice along the crystallographic  $a$ -axis. At a phase boundary between the high- and low-lithiated phases, interfacial lattice mismatch is inevitable as a result of the differential in unit cell dimensions, the anisotropy of the differentials (higher along the crystallographic  $b$ -direction than along the  $a$ - and  $c$ -directions), and considerable change in volume ( $\epsilon\text{-Li}_{0.3}\text{V}_2\text{O}_5$  has a unit cell volume *ca.* 1.66% higher than  $\alpha\text{-Li}_{0.1}\text{V}_2\text{O}_5$ ).<sup>15</sup> The stress distribution maps further portray the concentration of stress along domain boundaries, which can deleteriously impact diffusion kinetics and can further result in accumulated stresses and fracture. Indeed, regular striping of high- and low-lithiated phases has been predicted for  $\text{Li}_x\text{FePO}_4$  nanoparticles with a periodicity governed by the interfacial energy, particle width, and free energy differential between the homogeneous and phase-separated states as per:<sup>7,62</sup>

$$\lambda = \sqrt{\frac{2\gamma L_c}{\Delta f}} \quad (2)$$

where  $\lambda$  is the period of the striping,  $\gamma$  is the interfacial energy,  $L_c$  represents the particle width, and  $\Delta f$  is the free energy difference between the homogenous and phase-separated states.<sup>7</sup>

In this work, the observations of periodic striations in bent  $\text{V}_2\text{O}_5$  nanowires provide direct visualization of coupling between strain and spinodal decomposition in a thermodynamically controlled regime. The bend in the  $\text{V}_2\text{O}_5$  nanowire represents a structural perturbation that establishes a strain gradient within the nanowire. Anisotropic strain modifies the low- and high-lithiated phases ( $\alpha$ - and  $\epsilon\text{-Li}_x\text{V}_2\text{O}_5$ , respectively) to different extents, which in turn alters the degree of lattice incommensurability and thus the coherency strain resulting from the formation of a phase boundary. The bending-induced strain field thus represents an additional perturbation to the free energy landscape as sketched in Fig. 4A. The idle period ( $> 72$  h) separating the final delithiation step and the subsequent STXM measurements ensures that the system can phase separate in the presence of this strain. As will be discussed in

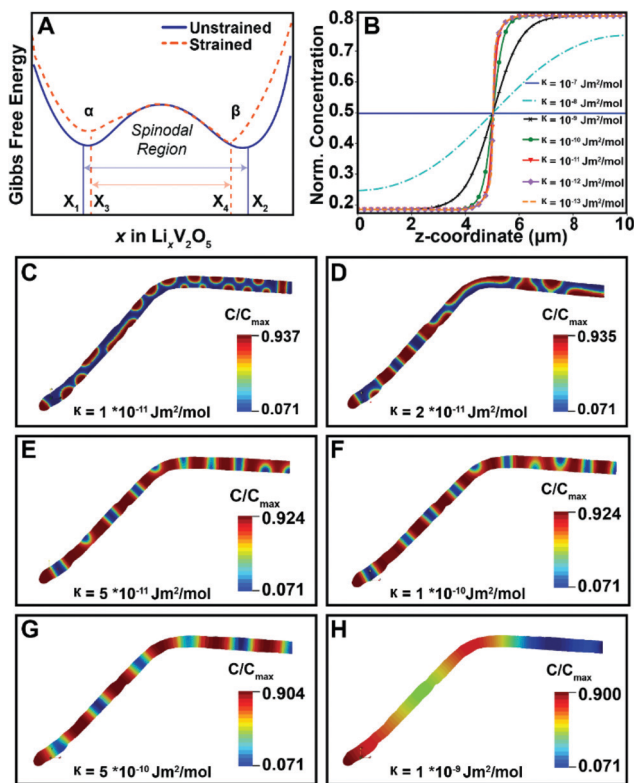


Fig. 4 Phase-field modeling of phase separation patterns. (A) Schematic depiction of a Gibbs free energy curve showing the phase separation of two distinct phases  $\alpha$ , and  $\beta$ , at  $x_1$  and  $x_2$  in  $\text{Li}_x\text{V}_2\text{O}_5$ , respectively. The structural distortion brought upon by the application of a bending-induced strain alters the relative stability of the two phases inequivalently (as illustrated by the orange-colored dotted line), and further narrows the spinodal region, which now occurs between  $x_3$  and  $x_4$ . (B) Plot illustrating the relationship between  $\kappa$  and the interfacial thickness (described by the  $z$ -coordinate which represents a dimension relative to the length of the particle). (C–H) Phase-field modeling for the mechanically coupled Cahn–Hilliard type diffusion for a particle whose geometry is derived from the nanowire image shown in Fig. 3. Each frame illustrates the phase-pattern at equilibrium in the presence of varying interface parameters,  $\kappa$ . With increasing  $\kappa$  the periodicity of the Li-rich and Li-poor domains become well defined and the interface formed between them more diffuse.

more detail below, spinodal decomposition and periodic striations are notably manifested during delithiation in a diffusion-limited regime, which is not subject to the nucleation constraints that are of paramount importance during lithiation.

To simulate the phase separation patterns, we have implemented a phase-field model for mechanically coupled Cahn–Hilliard type diffusion (Fig. 4).<sup>41,61</sup> Fig. 4C–G and Videos S1–S6 (ESI<sup>†</sup>) depict equilibrium concentration profiles in the presence of distinct interfacial energetics quantified by the gradient energy coefficient  $\kappa$ , which introduces an interfacial energy penalty that disfavors the growth of phase interfaces within the nanowire.<sup>41</sup> The free energy for this chemo-mechanically coupled process is introduced as a combination of the bulk chemical free energy (which depends on the local concentration); the interface free energy, which is a function of the concentration gradient; and the elastic energy which accounts

for coherency strain arising from lattice misfit:<sup>57</sup>

$$\psi = RTC_{\max}[c \ln c + (1 - c) \ln(1 - c) + \chi c(1 - c)] + \frac{1}{2}C_{\max}\kappa|\nabla c|^2 + \frac{1}{2}\sigma:\varepsilon^{\text{el}} \quad (3)$$

where  $R$  and  $T$  denote the gas constant and temperature, respectively, and  $C_{\max}$  is the maximum stoichiometric fraction of lithium in  $\text{Li}_x\text{V}_2\text{O}_5$ . Here,  $\chi$  is a coefficient representing the interaction between two phases, and  $\sigma$  and  $\varepsilon^{\text{el}}$  represent stress and strain, respectively.

By setting the derivative of the bulk energy terms (the first and the third terms on the right-hand side of eqn (3) to zero), one can determine the bulk equilibrium concentrations for the  $\alpha$  and  $\beta$  phase in the phase-separated state, which are denoted in eqn (4) by  $c_\alpha$  and  $c_\beta$ , respectively. The interface thickness  $s$  can be defined as a function of the interface parameter  $\kappa$  as follows:

$$s = (c_\beta - c_\alpha) \sqrt{\frac{\kappa}{2\Delta\psi^c}} \quad (4)$$

where  $\Delta\psi^c = \psi\left(\frac{c_\alpha + c_\beta}{2}\right)$  represents the chemical energy barrier required for the phase transformation.<sup>63</sup> From eqn (4), we see that for a given bulk free energy, interface thickness is proportional to the square root of  $\kappa$ . Fig. 4B depicts the evolution of the sharpness of the interface between the Li-poor and Li-rich interfaces as a function of  $\kappa$ .<sup>63</sup> Higher  $\kappa$  values lead to more diffuse interfaces between domains; sharp interfaces as experimentally observed in Fig. 3 are consistent with low or intermediate  $\kappa$  values. Snapshots of the  $\text{Li}_x\text{V}_2\text{O}_5$  nanowire with varying magnitudes of  $\kappa$  are shown in Fig. 4C–H; the relatively large range for  $\kappa$  in this work is intended to illustrate the role of the interfacial energy term in determining the energetically preferred phase separation morphology in the presence of geometric anisotropy. Fig. 4C and D show that small values of  $\kappa$  favor phase-separated Li-rich/Li-poor domains that are characterized by a plurality of thin interfaces (accessible as a result of the low energetic penalties) and oriented such that the interfacial energy of the system is minimized. In contrast, with increasing  $\kappa$ , the resulting patterns of Li-rich and Li-poor domains become periodically defined and the resulting phase interfaces are more diffuse following the relationship outlined in eqn (4). In addition to interfacial energetics, the energetically preferred interfaces are modified by the nanowire morphology as a result of geometric anisotropy.<sup>63</sup> Fig. 4C–H show that the domain size, shape, and orientation of lithiated domains are modified to different extents by geometry based on the magnitude of the interfacial energy (the apparent geometric effect becomes increasingly diminished with increasing  $\kappa$ ). Fig. 4D and the corresponding Video S2 (ESI<sup>†</sup>) best describe the experimentally observed domains shown in Fig. 3 which are characterized by moderately sharp interfaces. This value is in good agreement with previous reports on electrode materials based on transition-metal oxides that form coherent interfaces. In this system, it represents a regime wherein the effect of

bending is sufficiently large enough to alter otherwise periodic domains of Li-rich and Li-poor regions.<sup>7,64,65</sup>

Notably, the model examines the interplay of dimensionality, curvature, and  $\kappa$ , the interfacial parameter, but does not account for the change in the free energy differential between the Li-rich and Li-poor phases resulting from curvature-induced strain. Previous work has shown that the interfaces which minimize the overall interfacial energy may differ from those minimizing the volume-averaged coherency strain.<sup>66</sup> The elastic strain energy induced by the static bend makes an additional contribution to the system's free energy through altered structural motifs and distinctive chemical bonding, which necessarily translates to rearrangement of the free energy landscape. Indeed, the potency of strain applied either 'chemically' through doping,<sup>62,67–70</sup> or extrinsically through epitaxial mismatch has been demonstrated in materials exhibiting solid–solid phase transformations.<sup>68,71,72</sup> These results demonstrate that the efficacy of external perturbations in modifying phase separation patterns depends on the interplay between the intrinsic material properties that govern the energetically preferred interfaces and the geometry/curvature of the system.

### Imaging single-particle lithiation heterogeneities upon lithiation

As a point of comparison, a second nanowire with a similar radius of curvature and particle width has been examined to explore asymmetry in the phase separation patterns, but this time upon lithiation. The spectra and corresponding phase maps are shown in Fig. 5. Consistent with the greater overall extent of lithiation as compared to the delithiated particles shown in Fig. 3, the  $3d_{xy}$  feature (shown in Fig. 5B) at the V  $L_3$ -edge in both spectra are barely discernible, which indicates a high degree of lithiation. Based on comparison to standards (Fig. S3, ESI<sup>†</sup>), the spectral signatures indicate the formation of the highly lithiated  $\delta$ - $\text{Li}_x\text{V}_2\text{O}_5$  phase for the cluster 2 spectrum. This renormalization of the relative intensity of the  $t_{2g}$  and  $e_g^*$  features is discussed in greater detail above in light of the substantial alteration of the vanadium local coordination environment (Fig. S4, ESI<sup>†</sup>).<sup>42</sup> Therefore, based on the  $t_{2g}$  and  $e_g^*$  ratios and line shapes in O K-edge spectra, clusters 1 and 2 in Fig. 5A are assigned to  $\varepsilon$ - $\text{Li}_{0.7}\text{V}_2\text{O}_5$  and  $\delta$ - $\text{Li}_{0.9}\text{V}_2\text{O}_5$  phases, respectively. The latter structure, sketched in Fig. S1C (ESI<sup>†</sup>), is characterized by a large shift in the stacking sequence which results in a change in space group symmetry to *Amma* (hence the drastic change in O K-edge spectral shape which is a departure from the nearly linear change in the  $t_{2g}$  to  $e_g^*$  between  $\alpha$ - $\text{Li}_{0.1}\text{V}_2\text{O}_5$  and  $\varepsilon$ - $\text{Li}_{0.7}\text{V}_2\text{O}_5$  (Fig. S1E, ESI<sup>†</sup>)) and a volumetric expansion approaching 12.8% with respect to orthorhombic  $\text{V}_2\text{O}_5$  (Fig. S4, ESI<sup>†</sup> shows a magnified view of the distortion of the local structure).<sup>4,26</sup> Fig. 5F plots the corresponding quantitative composition map. Analogous to the nanowire in Fig. 3, phase separation is observed near the bend; however, there are no periodic striations of the Li-rich phase as in the case of the delithiated nanowire, and the phase domains span a relatively greater expanse. Fig. 5D shows that the bent region is on average less lithiated than the nanowire

ends.<sup>17</sup> Furthermore, the outer edge near the bend in the nanowire (which is likely under tension) is best described by the low lithiated component suggesting tensile strain applied along this crystallographic orientation hinders diffusion. While seemingly counterintuitive (many systems have increased diffusion under tensile strain),<sup>73,74</sup> this observation is consistent with recent work which demonstrates a highly lithiated "hot spot" centralized along a compressively strained region of a  $\text{V}_2\text{O}_5$  nanoparticle and is consistent with the increased diffusivity under a compressive strain along the crystallographic  $c$  direction observed by Pint and co-workers.<sup>17,26</sup> The results illustrated in Fig. 5 demonstrate the implications of strain for diffusion kinetics during lithiation.

The stress map plotted for the lithiated nanowire (Fig. 5G) shows that the highest regions of von Mises stress occur at the phase boundary between  $\varepsilon$ - $\text{Li}_{0.7}\text{V}_2\text{O}_5$  and  $\delta$ - $\text{Li}_{0.9}\text{V}_2\text{O}_5$ . Here the von Mises stress magnitudes are an order of magnitude larger than  $\alpha$ - $\varepsilon$ - $\text{Li}_x\text{V}_2\text{O}_5$  phase mixture shown in Fig. 3, which can be explained by the comparatively large rearrangement of the layer stacking during the  $\varepsilon$ - to  $\delta$ - $\text{Li}_x\text{V}_2\text{O}_5$  phase transition (Fig. S1E, ESI<sup>†</sup>) and the resulting greater lattice incommensurability.<sup>4,75</sup> Indeed the  $\varepsilon$ - to  $\delta$ - $\text{Li}_x\text{V}_2\text{O}_5$  phase transition is strongly anisotropic, characterized by a significant increase in the  $b$  lattice parameter with only modest changes to the  $a$  and  $c$  lattice parameters, and necessitates a shift in the stacking sequence along the crystallographic  $b$ -axis by half a unit cell length, thus enforcing a comparatively large rearrangement of the layer stacking as compared to the  $\alpha$ - to  $\varepsilon$ -phase transformation.<sup>4</sup> In both Fig. 3 and 5, the resulting stress profiles reflect the spatial distribution of differently lithiated domains.

The sharply distinct phase separation patterns and stress profiles observed for similar nanowire morphologies during lithiation and delithiation can be rationalized based on the distinctive nature of these processes. Lithiation, particularly at low C-rates, is a stochastic (or defect mediated) surface-reaction-limited process wherein random fluctuations have to be invoked to describe initial nucleation of the lithiated phase.<sup>26,49,76</sup> Lattice strain imposed by bending modifies nucleation probabilities as demonstrated by the localized Li-poor and Li-rich phases at and away from the origin of the bend, respectively in Fig. 5. Therefore, the observed phase separation pattern and accompanying misfit strain represent the dynamics of initial nucleation and further correspond to a metastable configuration reflective of reaction fronts initiated by specific surface nucleation events.<sup>26</sup> At high C-rates, or when nucleation restrictions no longer play a dominant role, a bulk-diffusion-limited regime is expected and is manifested in the form of core–shell phase separation<sup>77,78</sup> in particles above a critical size. The phase separation patterns will furthermore depend on the particle size since the magnitude of the nucleation barrier and the diffusion length scale with the surface-to-volume ratio and the particle radius, respectively.<sup>41,79–81</sup> Operando spectromicroscopy measurements of  $\text{LiFePO}_4$  nanoparticles illustrate that at high rates (2C), the Li composition maps reveal little or no heterogeneity across the different depths of discharge.<sup>49</sup> In contrast, during delithiation, the

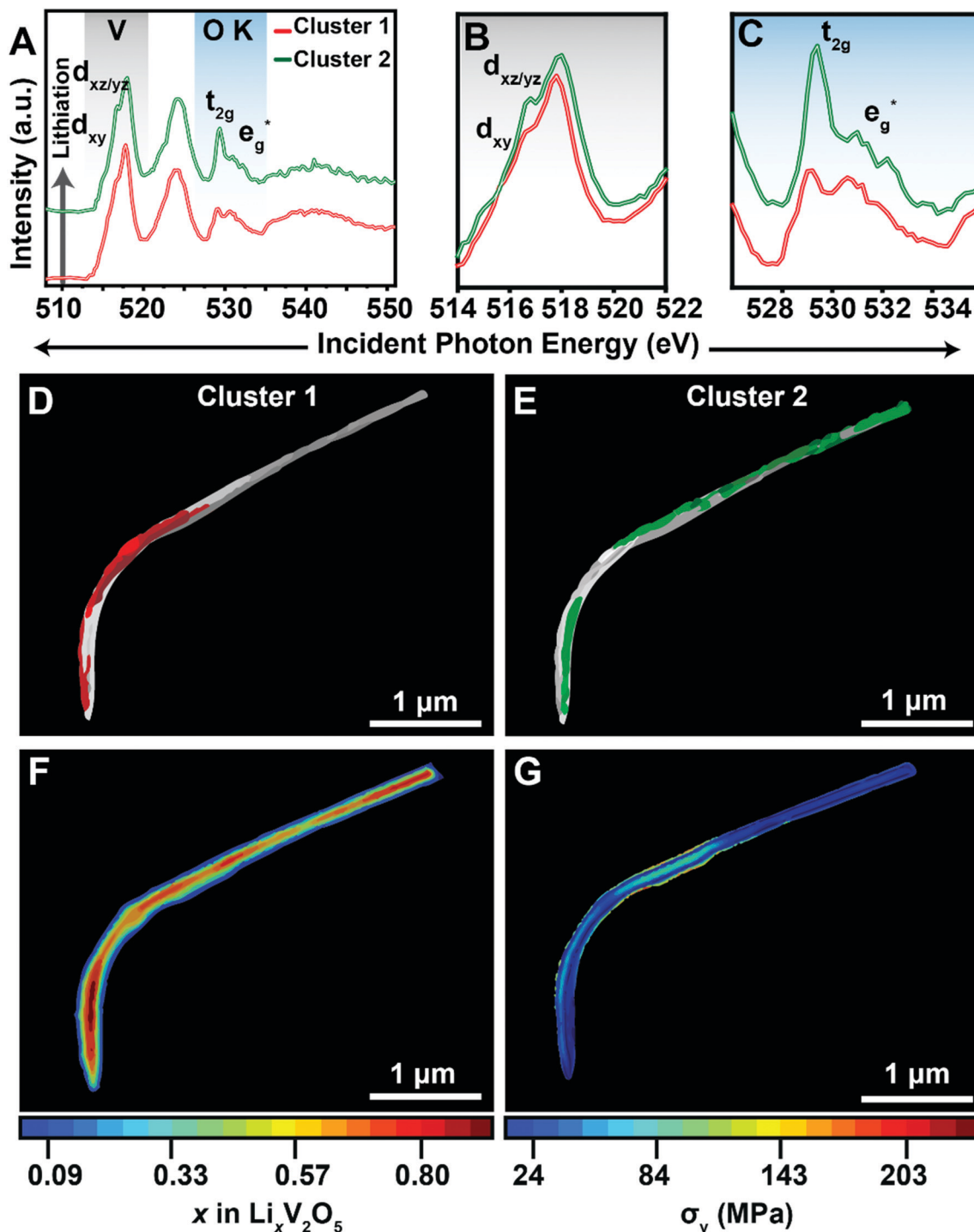


Fig. 5 Compositional domains and resulting stress gradients within a bent nanowire following lithiation. (A) Spectra obtained by averaging the spectral response of every pixel belonging to a cluster as differentiated by a combinatorial PCA/clustering process. Spectra are plotted in order of increasing average extent of lithiation (bottom to top). Panels (B and C) highlight the lithiation-induced changes across V  $L_{3-}$  and oxygen K-pre-edge regions, respectively. The drastic change in (C) for the  $\delta$ - $\text{Li}_{0.9}\text{V}_2\text{O}_5$  phase is a departure from the nearly linear change in the  $t_{2g}$  to  $e_g^*$  between  $\alpha$ - $\text{Li}_{0.1}\text{V}_2\text{O}_5$  and  $\varepsilon$ - $\text{Li}_{0.6}\text{V}_2\text{O}_5$  as a result of comparatively large rearrangement of the layer stacking during the  $\varepsilon$ - to  $\delta$ - $\text{Li}_x\text{V}_2\text{O}_5$  phase transition (Fig. S1E and S4, ESI†). The spatial orientation of each pixel contained in cluster 1 and cluster 2 is illustrated by red and green highlights in (D and E), respectively. The composition map as derived by the procedure detailed in the Materials and Methods sections for the chemically cycled bent nanowire during de-lithiation is shown in (F). The stress profile derived from the apparent heterogeneity is illustrated in (G).

degree of compositional inhomogeneity is much larger than at the onset of lithiation, giving rise to dramatically different local

current densities that further amplify diffusion inhomogeneities. In addition, the equilibrium phase mixture at the onset of

delithiation becomes destabilized by Li-ion extraction which forces the system to bifurcate into a new combination of the two stable phases as it re-enters the spinodal region.<sup>41,76</sup> In the absence of nucleation limitations, spinodal decomposition plays a dominant role during delithiation, allowing for the manifestation of phase separation motifs, which reflect the energetic trade-offs between the bulk homogenous free energy, the interfacial energy, and the elastic strain energy modified by geometric factors derived from the particle size and shape (Fig. 4 and eqn (4)).<sup>49,82</sup>

## Conclusions

Degenerative capacity loss resulting from interfacial delamination and active particle pulverization represents a significant obstacle to realizing the potential of Li-ion batteries in full measure. In brittle ceramics, which represent the vast majority of cathode materials, the accumulation of intercalation-induced stresses can be substantial, especially in phase-separating materials, despite the modest volumetric expansion that accompanies Li-ion insertion. Even for composite electrodes, considerable lithiation heterogeneity and accumulated stresses are evidenced in wafer curvature measurements of  $V_2O_5$  particles during electrochemical cycling. The origins of this heterogeneity and lattice strain have been elucidated using spectral signatures of differently lithiated domains to map phase separation and stress build-up within individual elastically deformed curved particles of  $V_2O_5$  during lithiation and delithiation. The coupling of geometry and finite size with interfacial energy and phase separation energies governs the phase-separation motifs observed during delithiation; high-resolution X-ray microscopy imaging reveals nanoscale self-organized striations of the Li-rich phase at the bend of the particle, manifesting a spinodal decomposition regime that is modified by curvature. Complementary phase-field models based on mechanically coupled Cahn–Hilliard type diffusion capture the characteristic striations and reveal that their organization and periodicity is modified by the magnitude of the interfacial parameter,  $\kappa$ . In contrast, during lithiation, a surface-reaction-limited nucleation and growth mechanism is dominant and stabilizes a metastable phase-separated configuration with distinctive lithiated domains at the two sides of the bend. The compressive and tensile stresses generated at either side of the coherent interface modify the Li-ion diffusivities of  $V_2O_5$  differently and further exacerbate the observed heterogeneities.<sup>83</sup>

The results presented here demonstrate the dynamic coupling between electrochemistry, mechanics, and particle geometry in determining phase separation and accumulated stresses and specifically implicate the morphology of phase boundaries in the intraparticle stress gradients that contribute to electrode degradation. The bending-driven alteration of phase separation patterns observed in this work illustrates that the same electrochemistry-mechanics mechanisms relating Li-ion diffusion to mesoscale mechanics can be leveraged by strain engineering to design electrode architectures with pre-determined diffusion characteristics and phase-separation motifs that

minimize intercalation-induced stresses (for instance, through the introduction of continuous curvature in nanobowl architectures).<sup>26</sup> In addition to enhanced transport kinetics, phase-separating materials stand to benefit from strain-driven alterations of thermodynamics of phase transformations and two-phase coexistence regimes. Architected electrodes that make use of pre-determined geometries or alternatively, “chemical” strain achieved by alloying can reduce the lattice mismatch resulting from phase boundaries, and in turn, minimize the miscibility gap of the coexisting phases and the energetic barrier required to initiate their transformation.<sup>67,84,85</sup> Analogously, phase transformations can be suppressed entirely by raising the coherency strain energy penalty beyond the threshold where two-phase coexistence is energetically preferred over a homogeneous metastable phase (*i.e.*, the energetic penalty resulting from the formation of an interface is larger than the energetic gain from spinodal decomposition).<sup>7,16,84</sup> Nanoscale and mesoscale designs that leverage both the kinetics of Li-ion diffusion and the thermodynamics of the subsequent phase transitions are paramount to controlling or entirely mitigating intercalation-induced transformations and their resulting stress implications. The ionic and electronic structure roadblocks observed for  $\alpha$ - $V_2O_5$  have many parallels in other transition metal oxides with strong electron correlation, making the principles gleaned here applicable to other systems with extended phase coexistence regimes.<sup>4,33,86</sup>

## Materials and methods

### Synthesis of $V_2O_5$ nanowires

Phase-pure single-crystalline  $V_2O_5$  nanowires were hydrothermally grown as reported in previous work<sup>45,46</sup> and range from 50 to 400 nm in width and span multiple microns in length.<sup>45</sup> Briefly, bulk  $\alpha$ - $V_2O_5$  particles (Sigma-Aldrich 99.5%) were hydrothermally reduced in a solution of water and 2-propanol (7 : 1 v/v) to yield  $V_3O_7 \cdot H_2O$  nanowires, which were subsequently oxidized and dehydrated by annealing at 350 °C in air over a period of 72 h to yield  $\alpha$ - $V_2O_5$  nanowires. Phase purity was confirmed by powder X-ray diffraction (XRD) (Fig. S2A, ESI<sup>†</sup>), and nanowire morphology was observed using scanning electron microscopy (SEM).

### Electrochemical and mechanical measurements

Electrodes were prepared using bulk  $V_2O_5$  [Sigma-Aldrich, 70 wt%], conductive carbon [Super C65 (MTI Corporation), 20 wt%], and binder [poly(vinylidene fluoride), 10 wt%] in *N*-methyl-2-pyrrolidone and casting the film onto a stainless steel substrate by spin coating. *Operando* electrochemical and mechanical measurements were performed using a two-electrode electrochemical test cell with a quartz viewing window (MTI Corporation) assembled in an Ar glovebox environment (with <1 ppm  $O_2$  and moisture levels). The cell comprised a lithium metal ribbon (99.9% trace metals basis, Sigma-Aldrich) anode, a Celgard 2400 separator (MTI Inc.), and a 1 M  $LiPF_6$  electrolyte (MTI Inc.) dissolved in a 1 : 1 (v/v)

mixture of ethylene carbonate: diethyl carbonate. Galvanostatic electrochemical measurements were performed on a PARSTAT MC Multichannel Potentiostat (Princeton Applied Research) at a 0.2C rate between 4–2 V vs. Li/Li<sup>+</sup>. A multi-beam optical stress sensor (MOS) from *k*-space Associates was used to monitor the curvature of the substrate ( $\Delta K$ ) during electrochemical cycling. Unwanted vibrations were minimized using a vibration isolation table.

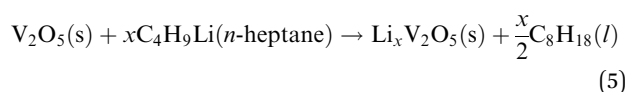
### Scanning electron microscopy and focused-ion beam deposition

SEM images were collected on a Tescan LYRA-3 model microscope equipped with a Schottky field-emission electron source and a low aberration conical objective lens. Prior to imaging, nanowires were drop-cast on a silicon nitride X-ray microscopy window, which was then affixed to a SEM sample holder by carbon tape. No surface coatings were used in order to preserve the integrity of the sample surface. Similarly, a low accelerating voltage (5 kV) was used to minimize any possible beam damage. Ion-beam-induced deposition was achieved on the same Tescan system equipped with a Ga liquid metal ion source and gas injection system for Pt deposition. Controlled deposition in well-defined areas was facilitated by the DrawBeam software module. A coincidence point was set at a 9 mm working distance, and the sample was oriented 55° from normal. A 30 kV accelerating voltage and was used for the ion optics.

### Chemical lithiation of V<sub>2</sub>O<sub>5</sub> nanowires on an X-ray microscopy substrate

The as-synthesized V<sub>2</sub>O<sub>5</sub> nanowires were dispersed *via* ultrasonication in 2-propanol (5 mg mL<sup>-1</sup>, for 10 min) and subsequently drop-cast onto a silicon nitride X-ray grid (Norcada location-tagged ‘holey’ TEM grids comprising a 200 nm thick silicon nitride film suspended on a 200 μm thick silicon frame) which was pre-cleaned by a UV/ozone cleaning method. As the solvent evaporates, the nanowires become physisorbed onto the surface of the grid. The dispersion of the nanowires was initially evaluated using an Olympus BX41 optical microscope. Before subjecting the grid to any chemical treatment (*i.e.*, lithiation/delithiation), a systematic grid search was performed to identify regions of interest and record the corresponding locations, enabling specific nanowires to be quickly imaged in subsequent STXM experiments (Fig. S2B, ESI†)

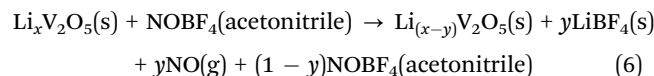
In order to preserve the integrity of the silicon nitride substrate, nanowire-containing X-ray grids were mechanically affixed in a home-built apparatus equipped with a linear guide rail to facilitate the controlled immersion of samples into solution with minimal handling. Lithiation of the as-prepared V<sub>2</sub>O<sub>5</sub> nanowires was achieved by direct reaction with a molar excess of *n*-butyllithium (0.01M)<sup>51</sup> in heptane for 3 min under in an inert glovebox environment as follows:



It is important to note that despite the large molar excess, limiting the reaction time facilitates incomplete lithiation of

the nanowires, facilitating analysis of heterogeneity. The lithiated nanowires were subsequently washed with copious amounts of anhydrous heptane to remove any excess unreacted *n*-butyllithium from the surface and prevent the formation of unwanted surficial Li<sub>x</sub>O<sub>y</sub> species. The grids were finally sealed under vacuum for transport to the synchrotron for STXM measurements.

A parallel set of samples was subsequently delithiated *via* immersion in a 0.01 M solution of nitrosonium tetrafluoroborate (NOBF<sub>4</sub>) solution<sup>87</sup> in acetonitrile for 3 min as per:



The particles were immersed in anhydrous acetonitrile to remove excess LiBF<sub>4</sub> from the surface. A total of five lithiation/delithiation treatments were performed (one cycle corresponds to V<sub>2</sub>O<sub>5</sub> → Li<sub>x</sub>V<sub>2</sub>O<sub>5</sub> → V<sub>2</sub>O<sub>5</sub>) with the final delithiation step (eqn (6)) leaving the nanowires in a ‘‘charged’’, or partially delithiated, state. In order to preserve the quality of the grid surface, each sample was maintained in an Ar environment throughout the entirety of the process and dried under Ar between each cycle.

### STXM experimental details and analysis workflow

STXM measurements were performed at the spectromicroscopy beamline 10D-1 of the Canadian Light Source in Saskatoon, SK utilizing a 7 mm generalized Apple II elliptically polarizing undulator source (EPU). Briefly, the incident X-ray source was focused to a sub 30 nm beam spot by a Fresnel zone-plate coupled with an order-sorting aperture to reduced unwanted diffraction orders. The focused beam spot was subsequently raster-scanned along a user-selected region of interest in increments determined by the target resolution for the measurements (35 nm). The incident X-ray energy was tuned *via* a 500 line mm<sup>-1</sup> monochromator to scan across the vanadium L- and oxygen K-edge energy range (*ca.* 508–560 eV). Transmission data were collected at every pixel and across the entire energy range with uniform dwell times (1 ms). A step size of 1 eV was used along the pre-edge and post-edge regions, and a 0.2 eV resolution was used across the V L<sub>2</sub>, V L<sub>3</sub>, and O K-edge resonances. The three-dimensional stack of images (position *x*, position *y*, and incident photon energy, *I*) were aligned along the spatial dimensions using a cross-correlation method contained within the aXis2000 software suite. The optical density matrix was obtained from the measured transmission images normalized by the incident spectrum acquired for a fully transmitting hole in the X-ray window.

Manual inspection of heterogeneity was performed by defining a real space region of adjacent pixels and averaging their spectral signature. Region-of-interest analyses were used to verify the results of the principal component analysis (PCA), cluster, and singular value decomposition (SVD) workflows. PCA and clustering were performed in MANTIS, a spectro-microscopy analysis program developed in Python.<sup>60</sup> Briefly, PCA was used to obtain a set of eigenimages and eigenspectra

from the covariance matrix. Once the  $n$  number of significant components that describe the non-noise variations in the data has been selected, pixels with similar scores in a mutually orthogonal  $n$ -dimensional space were grouped using k-means clustering. The spectra for each cluster are generated by taking the average pixel response at each energy and for every pixel contained in a cluster. Spectra derived from each cluster were referenced against previous theoretical and experimental reports to infer and assign values of  $x$  in  $\text{Li}_x\text{V}_2\text{O}_5$ . The number of clusters is increased or decreased in an iterative fashion such that the final quantity of clusters and their corresponding spectra represent distinct phases of  $\text{Li}_x\text{V}_2\text{O}_5$ .

### Compositional and von Mises stress maps

Thickness maps of each chemical component (as described by the set of  $S$  number of spectra from the cluster analysis) can be directly calculated by pseudo inversion in the form of

$$t_{S \times P} = (\mu_{N \times S})^+ D_{N \times P} \quad (7)$$

where  $t_{S \times P}$  represents a matched set of  $S$  thickness maps,  $\mu_{N \times S}^+$  is a pseudoinverse of the set of  $S$  absorption spectra, and  $D_{N \times P}$  is the optical density matrix.<sup>60,88</sup> Here, each pixel can be described by the superposition of its pixel value from each of the  $S$  number of thickness maps weighted by the stoichiometric value of  $x$  in  $\text{Li}_x\text{V}_2\text{O}_5$  assigned to the corresponding absorption spectrum as

$$X_i = (t_S x_S) + (t_{S-1} x_{S-1}) + (t_{S-2} x_{S-2}) \dots \quad (8)$$

where  $X_i$  is the concentration in pixel  $i$ ,  $t_s$  is the pixel value of pixel  $i$  in the thickness map for cluster number  $S$ , and  $x_S$  is the stoichiometric fraction of lithium  $x$  in  $\text{Li}_x\text{V}_2\text{O}_5$  assigned to cluster  $S$ .

The geometry of each nanowire was derived from the SVD-generated maps subjected to a Gaussian filter to remove noise. A high-fidelity representation of the nanowire geometry can be achieved by bilinear interpolation of the pixel data, which yields the continuous representation shown in Fig. 3F and 5F. A Marching Squares algorithm guided by a user-selected pixel-intensity-threshold (to accurately distinguish between the particle and background) facilitates the determination of the nanowire outline and creation of a finite element mesh from the open-source Gmsh code.<sup>89</sup> The resulting finite element mesh was used to solve for the distribution of stresses using the FEAP software package.<sup>90</sup> Linear isotropic material behavior was assumed together with a chemical eigenstrain model:

$$\sigma_{ij} = C_{ijkl} \varepsilon_{kl}^{\text{el}}, \quad (9)$$

$$\varepsilon_{kl}^{\text{el}} = \varepsilon_{kl} - \frac{\Omega c}{3} \delta_{kl} \quad (10)$$

wherein:  $\sigma_{ij}$  denotes the components of the symmetric second-order Cauchy stress tensor;  $C_{ijkl}$  denotes components of the fourth-order elasticity tensor which described the elastic material properties,  $\Omega$  is the partial molar volume of  $\text{Li}_x\text{V}_2\text{O}_5$  under insertion of Li (interpolated from previously reported unit cell parameters of lithiated orthorhombic  $\text{V}_2\text{O}_5$ <sup>35,40</sup>) and  $\delta_{kl}$

are the components of the unit tensor. The components of the symmetric second-order infinitesimal strain tensor are described by  $\varepsilon_{kl}$ , given as

$$\varepsilon_{ij} = \frac{1}{2}(u_{i,j} + u_{j,i}) \quad (11)$$

where  $u_i$  denotes the components of the displacement vector and where the notation  $(\cdot)_{,i}$  indicates a partial derivative with respect to the  $i$ -th spatial coordinate. Here the elastic strain denoted by  $\varepsilon_{kl}^{\text{el}}$  is directly correlated to stress. For finite element simulations, the composition (initially determined by analysis of the V L- and O K-spectral regions and subsequently expressed by the image conversion process discussed in the above sections) was employed as a constant field, causing eigenstrain according to eqn (10). For simplicity, constant concentration-independent elastic parameters and a constant partial molar volume were approximated. A Young's modulus of  $E = 43$  GPa, a Poisson's ratio of  $\nu = 0.3$ , and a partial molar volume of  $\Omega = 2.415 \times 10^{-6} \text{ m}^3 \text{ mol}^{-1}$  were used as input in the finite element simulations.<sup>91</sup> In order to exclude rigid body displacements, the displacement components were constrained normal to the nanowire edges along the image borders. The resulting stresses and strains were finally transformed using standard techniques from the Cartesian coordinate frame to a nanowire-aligned planar coordinate system.

### Phase-field modeling of diffusion gradients across distinct interfacial energy terms

The system free energy for the chemo-mechanical coupling can be expressed as follows:

$$\psi = \psi^c + \psi^i + \psi^e \quad (12)$$

where  $\psi^c$ ,  $\psi^i$  and  $\psi^e$  denote the chemical free energy, the interface free energy, and the elastic free energy, respectively, as follows:

$$\psi^c = RTC_{\text{max}}[c \ln c + (1 - c) \ln(1 - c) + \chi c(1 - c)] \quad (13)$$

$$\psi^i = \frac{1}{2} C_{\text{max}} \kappa |\nabla c|^2 \quad (14)$$

$$\psi^e = \frac{1}{2} \sigma : \varepsilon^{\text{el}} \quad (15)$$

Therefore, the chemical potentials and the stress can be found below:

$$\mu^c = RT[\ln c - \ln(1 - c) + \chi(1 - 2c)]. \quad (16)$$

$$\mu^i = -\kappa \Delta c \quad (17)$$

$$\mu^e = \frac{\partial \psi^e}{\partial c} = -\Omega \sigma_{\text{h}} \quad (18)$$

and stress

$$\sigma = \frac{\partial \psi^e}{\partial \varepsilon} = C_{ijkl} \varepsilon_{kl}^{\text{el}} \quad (19)$$

where  $\Omega$  is the partial molar volume, and where  $\sigma_{\text{h}} = \frac{\sigma_{ii}}{3}$  is the hydrostatic stress.

As such, the linear moment balance and the mass conservation of lithium inside the nanowire can be expressed as:

$$\nabla \cdot \sigma = 0 \quad (20)$$

$$\frac{\partial c}{\partial t} = \nabla \cdot (M \nabla \mu) \quad (21)$$

$$\mu = \mu^e + \mu^i + \mu^e \quad (22)$$

where  $M = Dc(1 - c)$  is the mobility term. The related boundary conditions are:

$$u = u_0 \text{ on } \Gamma_u \quad (23)$$

$$-M \nabla \mu \cdot n = J_0 \text{ on } \Gamma_j \quad (24)$$

where  $u_0$  is the prescribed displacement on boundary  $\Gamma_u$ , and where  $J_0$  is the applied flux for the lithiation process. For the reaction:  $\text{Li} \rightleftharpoons \text{Li}^+ + \text{e}^-$ ,  $J_0$  can be described as:

$$J_0 = k_s(1 - c)\sqrt{\mu} \left[ \exp\left(\frac{1}{2} \frac{\mu}{RT}\right) - \exp\left(-\frac{1}{2} \frac{\mu}{RT}\right) \right] \quad (25)$$

where  $k_s$  is the reaction rate.

## Author contributions

D. A. S., J. L. A., B.-X. X. and S. B. contributed to the experimental design. D. A. S. contributed X-ray diffraction and scanning electron microscopy measurements. P. S. and B.-X. X. contributed compositional and strain maps and modeling. Y. B. and B.-X. X. contributed to the phase field modeling. Y. L., Y. Z., and M. P. contributed to the multi-beam optical stress sensor measurements. D. A. S. synthesized and chemically lithiated nanowire samples. D. A. S. and J. L. A. collected scanning transmission X-ray microscopy data. D. A. S. analyzed and processed (ROI, PCA, SVD, thickness maps) scanning transmission X-ray microscopy data. D. A. S., B.-X. X., and S. B. wrote the paper.

## Conflicts of interest

The authors declare no competing interests.

## Acknowledgements

A large portion of the research described in this article was performed at the Canadian Light Source (SM beamline), which is supported by the Natural Sciences and Engineering Research Council of Canada, the National Research Council Canada, the Canadian Institutes of Health Research, the Province of Saskatchewan, Western Economic Diversification Canada, and the University of Saskatchewan. We thank Dr Jian Wang at beamline 10ID1 of the Canadian Light Source for support and for STXM data collection. The use of the TAMU Materials Characterization facility is further acknowledged. This study is based on work supported by the National Science Foundation under DMR 1809866. D. A. S. acknowledges support from a

National Science Foundation Graduate Research Fellowship under grant number 1746932. J. L. A. acknowledges support from a NASA Space Technology Research fellowship under grant number 80NSSC17K0182. P. S. and B.-X. X. acknowledge the German Science Foundation for the financial support on the project STE2350/1-1 with the number 398072825. M. P. acknowledges support from NSF under DMR 1944674.

## Notes and references

- 1 J. B. Goodenough and K.-S. Park, *J. Am. Chem. Soc.*, 2013, **135**, 1167–1176.
- 2 M. Li, J. Lu, Z. Chen and K. Amine, *Adv. Mater.*, 2018, **30**, 1800561.
- 3 J. Wu, Z. Zhuo, X. Rong, K. Dai, Z. Lebens-Higgins, S. Sallis, F. Pan, L. F. J. Piper, G. Liu, Y. Chuang, Z. Hussain, Q. Li, R. Zeng, Z. Shen and W. Yang, *Sci. Adv.*, 2020, **6**, eaaw3871.
- 4 L. R. De Jesus, J. L. Andrews, A. Parija and S. Banerjee, *ACS Energy Lett.*, 2018, **3**, 915–931.
- 5 D. Eum, B. Kim, S. J. Kim, H. Park, J. Wu, S.-P. Cho, G. Yoon, M. H. Lee, S.-K. Jung, W. Yang, W. M. Seong, K. Ku, O. Tamwattana, S. K. Park, I. Hwang and K. Kang, *Nat. Mater.*, 2020, **19**, 419–427.
- 6 H. Liu, F. C. Strobridge, O. J. Borkiewicz, K. M. Wiaderek, K. W. Chapman, P. J. Chupas and C. P. Grey, *Science*, 2014, **344**, 1252817.
- 7 D. A. Cogswell and M. Z. Bazant, *ACS Nano*, 2012, **6**, 2215–2225.
- 8 L. R. De Jesus, Y. Zhao, G. A. Horrocks, J. L. Andrews, P. Stein, B.-X. B. Xu and S. Banerjee, *J. Mater. Chem. A*, 2017, **5**, 20141–20152.
- 9 G. R. Hardin, Y. Zhang, C. D. Fincher and M. Pharr, *JOM*, 2017, **69**, 1519–1523.
- 10 N. Kotak, P. Barai, A. Verma, A. Mistry and P. P. Mukherjee, *J. Electrochem. Soc.*, 2018, **165**, A1064–A1083.
- 11 J. A. Lewis, J. Tippens, F. J. Q. Cortes and M. T. McDowell, *Trends Chem.*, 2019, **1**, 845–857.
- 12 A. Mukhopadhyay and B. W. Sheldon, *Prog. Mater. Sci.*, 2014, **63**, 58–116.
- 13 P. Zuo and Y. P. Zhao, *Phys. Chem. Chem. Phys.*, 2015, **17**, 287–297.
- 14 M. Pharr, Z. Suo and J. J. Vlassak, *Nano Lett.*, 2013, **13**, 5570–5577.
- 15 Y. Zhang, Y. Luo, C. Fincher, S. Banerjee and M. Pharr, *J. Mater. Chem. A*, 2019, **7**, 23922–23930.
- 16 Y. Zhao, P. Stein, Y. Bai, M. Al-Siraj, Y. Yang and B. X. Xu, *J. Power Sources*, 2019, **413**, 259–283.
- 17 N. Muralidharan, C. N. Brock, A. P. Cohn, D. Schauben, R. E. Carter, L. Oakes, D. G. Walker and C. L. Pint, *ACS Nano*, 2017, **11**, 6243–6251.
- 18 R. Xu and K. Zhao, *J. Electrochem. Energy Convers. Storage*, 2016, **13**, 030803.
- 19 M. Wolf, B. M. May and J. Cabana, *Chem. Mater.*, 2017, **29**, 3347–3362.
- 20 M. T. McDowell, I. Ryu, S. W. Lee, C. Wang, W. D. Nix and Y. Cui, *Adv. Mater.*, 2012, **24**, 6034–6041.

- 21 X. H. Liu, L. Zhong, S. Huang, S. X. Mao, T. Zhu and J. Y. Huang, *ACS Nano*, 2012, **6**, 1522–1531.
- 22 K. D. Kepler, J. T. Vaughney and M. M. Thackeray, *J. Power Sources*, 1999, **81–82**, 383–387.
- 23 T. Li, Y. L. Cao, X. P. Ai and H. X. Yang, *J. Power Sources*, 2008, **184**, 473–476.
- 24 S. Chen, P. Bao, X. Huang, B. Sun and G. Wang, *Nano Res.*, 2014, **7**, 85–94.
- 25 L. Li, U. Steiner and S. Mahajan, *J. Mater. Chem.*, 2010, **20**, 7131.
- 26 J. L. Andrews, P. Stein, D. A. Santos, C. J. Chalker, L. R. De Jesus, R. D. Davidson, M. A. Gross, M. Pharr, J. D. Batteas, B.-X. Xu and S. Banerjee, *Matter*, 2020, **3**, DOI: 10.1016/j.matt.2020.08.030.
- 27 W. Ming, Z. F. Wang, M. Zhou, M. Yoon and F. Liu, *Nano Lett.*, 2016, **16**, 404–409.
- 28 Z. Liu, J. Wu, W. Duan, M. G. Lagally and F. Liu, *Phys. Rev. Lett.*, 2010, **105**, 016802.
- 29 Z. Dai, L. Liu and Z. Zhang, *Adv. Mater.*, 2019, **31**, 1805417.
- 30 J. L. Andrews, D. A. Santos, M. Meyyappan, R. S. Williams and S. Banerjee, *Trends Chem.*, 2019, **1**, 711–726.
- 31 S. Kim, S. J. Choi, K. Zhao, H. Yang, G. Gobbi, S. Zhang and J. Li, *Nat. Commun.*, 2016, **7**, 10146.
- 32 M. S. Whittingham, *J. Electrochem. Soc.*, 1976, **123**, 315–320.
- 33 N. A. Chernova, M. Roppolo, A. C. Dillon and M. S. Whittingham, *J. Mater. Chem.*, 2009, **19**, 2526–2552.
- 34 P. M. Marley, G. A. Horrocks, K. E. Pelcher and S. Banerjee, *Chem. Commun.*, 2015, **51**, 5181–5198.
- 35 R. J. Cava, A. Santoro, D. W. Murphy, S. M. Zahurak, R. M. Fleming, P. Marsh and R. S. Roth, *J. Solid State Chem.*, 1986, **65**, 63–71.
- 36 R. Enjalbert and J. Galy, *Acta Crystallogr., Sect. C: Cryst. Struct. Commun.*, 1986, **42**, 1467–1469.
- 37 L. R. De Jesus, P. Stein, J. L. Andrews, Y. Luo, B.-X. X. Xu and S. Banerjee, *Mater. Horiz.*, 2018, **5**, 486–498.
- 38 C. Delmas, H. Cognacauradou, J. Cocciantelli, M. Menetrier and J. Doumerc, *Solid State Ionics*, 1994, **69**, 257–264.
- 39 C. Delmas and H. Cognac-Auradou, *J. Power Sources*, 1995, **54**, 406–410.
- 40 D. W. Murphy, P. A. Christian, F. J. Disalvo and J. V. Waszczak, *Inorg. Chem.*, 1979, **18**, 2800–2803.
- 41 Y. Zhao, L. R. De Jesus, P. Stein, G. A. Horrocks, S. Banerjee and B. X. Xu, *RSC Adv.*, 2017, **7**, 41254–41264.
- 42 L. R. De Jesus, G. A. Horrocks, Y. Liang, A. Parija, C. Jaye, L. Wangoh, J. Wang, D. A. Fischer, L. F. J. Piper, D. Prendergast and S. Banerjee, *Nat. Commun.*, 2016, **7**, 12022.
- 43 Y. Luo, L. R. De Jesus, J. L. Andrews, A. Parija, N. Flerer, D. J. Robles, P. P. Mukherjee and S. Banerjee, *ACS Appl. Mater. Interfaces*, 2018, **10**, 30901–30911.
- 44 J. Wang, A. P. Hitchcock, C. Karunakaran, A. Prange, B. Franz, T. Harkness, Y. Lu, M. Obst and J. Hormes, *AIP Conf. Proc.*, 2010, **1365**, 215–218.
- 45 G. A. Horrocks, M. F. Likely, J. M. Velazquez and S. Banerjee, *J. Mater. Chem. A*, 2013, **1**, 15265.
- 46 G. A. Horrocks, E. J. Braham, Y. Liang, L. R. De Jesus, J. Jude, J. M. Velázquez, D. Prendergast and S. Banerjee, *J. Phys. Chem. C*, 2016, **120**, 23922–23932.
- 47 G. G. Stoney, *Proc. R. Soc. London, Ser. A*, 1909, **82**, 172–175.
- 48 Y. Li, H. Chen, K. Lim, H. D. Deng, J. Lim, D. Fraggadakis, P. M. Attia, S. C. Lee, N. Jin, J. Moškon, Z. Guan, W. E. Gent, J. Hong, Y.-S. Yu, M. Gaberšček, M. S. Islam, M. Z. Bazant and W. C. Chueh, *Nat. Mater.*, 2018, **17**, 915–922.
- 49 J. Lim, Y. Li, D. H. Alsem, H. So, S. C. Lee, P. Bai, D. A. Cogswell, X. Liu, N. Jin, Y. S. Yu, N. J. Salmon, D. A. Shapiro, M. Z. Bazant, T. Tylliszczak and W. C. Chueh, *Science*, 2016, **353**, 566–571.
- 50 A. P. Hitchcock, *J. Electron Spectrosc. Relat. Phenom.*, 2015, **200**, 49–63.
- 51 M. S. Whittingham and M. B. Dines, *J. Electrochem. Soc.*, 1977, **124**, 1387.
- 52 Q. Huang, H. Li, M. Grätzel and Q. Wang, *Phys. Chem. Chem. Phys.*, 2013, **15**, 1793–1797.
- 53 D. Gupta and G. M. Koenig, *J. Electrochem. Soc.*, 2020, **167**, 020537.
- 54 C. Kuss, M. Carmant-Dérival, N. D. Trinh, G. Liang and S. B. Schougaard, *J. Phys. Chem. C*, 2014, **118**, 19524–19528.
- 55 D. Maganas, M. Roemelt, M. Hävecker, A. Trunschke, A. Knop-Gericke, R. Schlögl and F. Neese, *Phys. Chem. Chem. Phys.*, 2013, **15**, 7260–7276.
- 56 G. A. Horrocks, L. R. De Jesus, J. L. Andrews and S. Banerjee, *JOM*, 2017, **69**, 1469–1477.
- 57 L. R. De Jesus, Y. Zhao, G. A. Horrocks, J. L. Andrews, P. Stein, B.-X. B. Xu and S. Banerjee, *J. Mater. Chem. A*, 2017, **5**, 20141–20152.
- 58 C. Shao, Y. Tian, Z. Dong, J. Gao, Y. Gao, X. Jia, G. Guo, X. Wen, C. Jiang and X. Zhang, *Am. J. Biomed. Sci.*, 2012, **4**, 85–101.
- 59 G. Ivosev, L. Burton and R. Bonner, *Anal. Chem.*, 2008, **80**, 4933–4944.
- 60 M. Lerotic, R. Mak, S. Wirick, F. Meirer and C. Jacobsen, *J. Synchrotron Radiat.*, 2014, **21**, 1206–1212.
- 61 Y. Zhao, B.-X. Xu, P. Stein and D. Gross, *Comput. Methods Appl. Mech. Eng.*, 2016, **312**, 428–446.
- 62 N. Meethong, H. Y. S. Huang, S. A. Speakman, W. C. Carter and Y. M. Chiang, *Adv. Funct. Mater.*, 2007, **17**, 1115–1123.
- 63 Y. Zhao, P. Stein and B. X. Xu, *Comput. Methods Appl. Mech. Eng.*, 2015, **297**, 325–347.
- 64 D. Morgan, A. Van der Ven and G. Ceder, *Electrochem. Solid-State Lett.*, 2004, **7**, 2003–2005.
- 65 M. Tang, J. F. Belak and M. R. Dorr, *J. Phys. Chem. C*, 2011, **115**, 4922–4926.
- 66 A. Abdollahi, O. Akyildiz, R. Malik, K. Thornton and G. Ceder, *J. Mater. Chem. A*, 2014, **2**, 15437–15447.
- 67 F. Omenya, N. A. Chernova, R. Zhang, J. Fang, Y. Huang, F. Cohen, N. Dobrzynski, S. Senanayake, W. Xu and M. S. Whittingham, *Chem. Mater.*, 2013, **25**, 85–89.
- 68 S. Catalano, M. Gibert, J. Fowlie, J. Íñiguez, J.-M. Triscone and J. Kreisel, *Rep. Prog. Phys.*, 2018, **81**, 046501.
- 69 E. J. Braham, D. Sellers, E. Emmons, R. Villarreal, H. Asayesh-Ardakani, N. A. Flerer, K. E. Farley, R. Shahbazian-Yassar, R. Arròyave, P. J. Shamberger and S. Banerjee, *Chem. Mater.*, 2018, **30**, 214–224.
- 70 L. Whittaker, T.-L. Wu, C. J. Patridge, G. Sambandamurthy and S. Banerjee, *J. Mater. Chem.*, 2011, **21**, 5580.

- 71 D. Preziosi, L. Lopez-Mir, X. Li, T. Cornelissen, J. H. Lee, F. Trier, K. Bouzehouane, S. Valencia, A. Gloter, A. Barthélémy and M. Bibes, *Nano Lett.*, 2018, **18**, 2226–2232.
- 72 M. Yang, Y. Yang, B. Hong, L. Wang, K. Hu, Y. Dong, H. Xu, H. Huang, J. Zhao, H. Chen, L. Song, H. Ju, J. Zhu, J. Bao, X. Li, Y. Gu, T. Yang, X. Gao, Z. Luo and C. Gao, *Sci. Rep.*, 2016, **6**, 23119.
- 73 J. Lee, S. J. Pennycook and S. T. Pantelides, *Appl. Phys. Lett.*, 2012, **101**, 033901.
- 74 C. Tealdi, J. Heath and M. S. Islam, *J. Mater. Chem. A*, 2016, **4**, 6998–7004.
- 75 R. Baddour-Hadjean, E. Raekelboom and J. P. Pereira-Ramos, *Chem. Mater.*, 2006, **18**, 3548–3556.
- 76 M. Z. Bazant, *Faraday Discuss.*, 2017, **199**, 423–463.
- 77 A. N. Mistry, K. Smith and P. P. Mukherjee, *ACS Appl. Mater. Interfaces*, 2018, **10**, 6317–6326.
- 78 D. Fraggedakis, N. Nadkarni, T. Gao, T. Zhou, Y. Zhang, Y. Han, R. M. Stephens, Y. Shao-Horn and M. Z. Bazant, *Energy Environ. Sci.*, 2020, **13**, 2142.
- 79 D. A. Cogswell and M. Z. Bazant, *Electrochem. Commun.*, 2018, **95**, 33–37.
- 80 Y. Li, F. El Gabaly, T. R. Ferguson, R. B. Smith, N. C. Bartelt, J. D. Sugar, K. R. Fenton, D. A. Cogswell, A. L. D. Kilcoyne, T. Tyliszczak, M. Z. Bazant and W. C. Chueh, *Nat. Mater.*, 2014, **13**, 1149–1156.
- 81 Y.-S. Yu, C. Kim, D. A. Shapiro, M. Farmand, D. Qian, T. Tyliszczak, A. L. D. Kilcoyne, R. Celestre, S. Marchesini, J. Joseph, P. Denes, T. Warwick, F. C. Strobridge, C. P. Grey, H. Padmore, Y. S. Meng, R. Kostecki and J. Cabana, *Nano Lett.*, 2015, **15**, 4282–4288.
- 82 Y. Zhu and C. Wang, *J. Power Sources*, 2011, **196**, 1442–1448.
- 83 M. G. Boebinger, D. Yeh, M. Xu, B. C. Miles, B. Wang, M. Papakyriakou, J. A. Lewis, N. P. Kondekar, F. J. Q. Cortes, S. Hwang, X. Sang, D. Su, R. R. Unocic, S. Xia, T. Zhu and M. T. McDowell, *Joule*, 2018, **2**, 1783–1799.
- 84 A. Van der Ven, K. Garikipati, S. Kim and M. Wagemaker, *J. Electrochem. Soc.*, 2009, **156**, A949.
- 85 H. H. Chang, C. C. Chang, H. C. Wu, M. H. Yang, H. S. Sheu and N. L. Wu, *Electrochem. Commun.*, 2008, **10**, 335–339.
- 86 M. Brahlek, L. Zhang, J. Lapano, H. T. Zhang, R. Engel-Herbert, N. Shukla, S. Datta, H. Paik and D. G. Schlom, *MRS Commun.*, 2017, **7**, 27–52.
- 87 K. T. Lee, T. N. Ramesh, F. Nan, G. Botton and L. F. Nazar, *Chem. Mater.*, 2011, **23**, 3593–3600.
- 88 C. Jacobsen, *X-ray Spectromicroscopy*, Cambridge University Press, 2019.
- 89 C. Geuzaine and J.-F. F. Remacle, *Int. J. Numer. Methods Eng.*, 2009, **79**, 1309–1331.
- 90 R. L. Taylor, FEAP – finite element analysis program, 2014, <http://www.ce.berkeley.edu/projects/feap>.
- 91 B. Sipos, M. Duchamp, A. Magrez, L. Forró, N. Barišić, A. Kis, J. W. Seo, F. Bieri, F. Krumeich, R. Nesper and G. R. Patzke, *J. Appl. Phys.*, 2009, **105**, 074317.